



Giovanni Corsi · Francesco Battista · Paolo Gualtieri · Stefano Vidoli

Effect of realistic distributed loads on the bi-stable behavior of a pre-stressed aileron

Received: 23 September 2023 / Revised: 11 December 2023 / Accepted: 5 January 2024
© The Author(s) 2024

Abstract We study both experimentally and numerically the aeroelastic response of a pre-stressed curved aileron in a high Reynolds number flow undisturbed at infinity. The structure is designed to have a peculiar nonlinear behavior. Specifically, the aileron has only one stable equilibrium when the external forces are vanishing, but it is bistable when distributed aerodynamic loads are applied. Hence, for sufficiently high fluid velocities, another equilibrium branch is possible. We test a prototype of such an aileron in a wind tunnel. A sudden change (snap) of the shell configuration is observed when the fluid velocity exceeds a critical threshold: the snapped configuration is characterized by sensibly lower drag. However, when the velocity is reduced to zero, the structure recovers its initial shape. A similar nonlinear behavior can have important applications for drag-reduction strategies since the transition between a bluff body-like and a slender body-like behavior is controlled by the free-stream fluid velocity and does not require any external actuation.

1 Introduction

A promising research paradigm in recent years has been the use of smart (or responsive) materials and structures, as enhancements to the functions of machines, or, in some cases, to replicate some of these functions altogether [1]. Fields where this paradigm has found many applications have been, among others, robotics [2] and aeronautics [3–6]. The functions that these materials allow can be divided into two broad categories [7]: energy-related, concerning applications such as energy harvesting or dissipation [8], and motion-related. One particular advantage is that these functions can usually be performed with reduced complexity of the final system, in that there is less need for actuating machinery, or complex control systems (if passive actuation is used). These applications can be obtained by taking advantage of the characteristics of the materials, such as memory shape alloys [9], hydrogels, elastomers, or polymers [10]. A valuable alternative consists in exploiting mechanical processes, such as the occurrence of instabilities. A great example of this is buckling [7, 11], an elastic instability that gives place to high deformations and sudden energy release, and can be exploited for

G. Corsi (✉) · S. Vidoli
Dipartimento di Ingegneria Strutturale e Geotecnica, Sapienza Università di Roma, Via Eudossiana, 18, Rome 00184, Italy
E-mail: giovanni.corsi@uniroma1.it

S. Vidoli
E-mail: stefano.vidoli@uniroma1.it

F. Battista · P. Gualtieri
Dipartimento di Ingegneria Meccanica e Aerospaziale, Sapienza Università di Roma, Via Eudossiana, 18, Rome 00184, Italy
E-mail: francesco.battista@uniroma1.it

P. Gualtieri
E-mail: paolo.gualtieri@uniroma1.it

both energy harvesting applications, motility, or design for actuators, among others. To induce such mechanical processes, an interesting approach is that of taking advantage of both the characteristics of the material and the geometry of the structure. For example, thin shells, when pre-stressed (e.g., by inelastic deformation during the production process), can have a spontaneous curvature and multi-stable behavior [12], which can be actuated to obtain complex motions [13] or yet again for energy harvesting applications. We remark in particular the development of simplified (i.e., low number of degrees of freedom) analytical models for such shells: in [14] a two-parameter model for shells with cylindrical natural configuration is given, and conditions for the existence of two stable configurations are investigated. The spontaneous curvature is due to the choice of the composite material of the shells. In [15], the same problem is studied when curvature is due to residual stresses. An analytical model for the prediction of bistability in composite shells is also developed, and tested both numerically and experimentally in [16], while in [17] a simplified analytical approach is used in the context of buckling instability of beams. In this work, we consider the case of a morphing shell, see [18], with application in the context of aerodynamics. These shells are such that they have a pseudo-conical natural configuration and, when clamped on one of the sides, tend to assume a curved shape, with possible bi-stable behavior when the initial curvature is chosen accordingly. This behavior is described with a reduced model [19], obtained with a different approach with respect to the ones introduced above, which takes into account the clamping of one of the sides. The use of bistable structures has been considered already in aeronautics [20,21], for example, for the alleviation of excessive aerodynamic loads [22]. In this regard, we note some of the advantages of our approach, and the particular features of the structure presented: the goal is to exploit the aerodynamic drag as actuation, inducing the bistable behavior after a critical loading threshold, obtaining sudden shape changes with consequent drag reduction. The system can be tuned to any critical load [18] and to the desired multi-stable behavior by simply changing the starting geometry before clamping and, thus, is very versatile compared to other usual applications when the material and geometry both have to be fine-tuned for each particular application. Furthermore, since actuation is due to the aerodynamic load alone, there is no need for complex actuations, such as heating, fluid supply, or chemical reactions. The dependence of the behavior on the load also means that the snap-through of the structure is trivially reversible: when the load decreases (that is, deceleration of the external flow) under a certain threshold, the structure snaps back to its original configuration. This makes the shell an excellent example of a smart structure in the context of aeroelasticity. It should be emphasized that the structure is not bistable if a load is not applied: it will be shown that applying a load at the tip, after the shell is clamped at one of the sides, and increasing the force progressively, such a morphing shell can deform and snap-through, due to the emergence of a second stable configuration only after a certain load threshold. This capability with a simple loading is easy to demonstrate. The purpose of this work is to demonstrate the feasibility of this approach in a more complex application, that is when the structure is under a realistic aerodynamic load. Such a load can be generated, for example, when the shell is mounted on a vehicle that moves at increasing speed: the aerodynamic drag generated acts as an actuating force and could induce, in suitable conditions, snap-through. It remains to prove that with this complex load, the desired behavior is still achieved, since the fluid stresses act as a distributed rather than concentrated load. To do this, we study the problem both experimentally and numerically. The first part of the study is experimental: a prototype of this shell, fabricated with lamina of composite material, was studied in the wind tunnel, subject to increasing aerodynamic loads generated by a uniform free-stream. The numerical study is a simulation of the aeroelastic problem with a quasi-static approach: the distributed aerodynamic load is computed for given stream velocity by steady-state RANS (Reynolds Average Navier–Stokes) simulations. The fluid stresses are used in a structural solver that provides the configuration of the aileron thus closing the aeroelastic loop. We show that the coupled fluid–structure system has a critical velocity that causes the snap-through observed experimentally. In this way, we fully explore the application of a promising smart structure in the aeroelastic context. This study represents an addition to the literature on the topic of drag reduction through shape reconfiguration [23–26]; the studied behavior can have many interesting uses, such as the already mentioned case of load alleviation over a certain drag threshold, as well as complex shape changes and energy harvesting. Moreover, the results will confirm the feasibility of using reduced models for the description of the (nonlinear) structural response to aerodynamic loads. In Sect. 2, the problem is stated in more detail. In Sect. 3, we report the features of the structure, the experimental setup, and the details of our numerical method. In Sect. 4, we report the results of the experimental study, the numerical results, and their comparison with the experimental ones. We draw conclusions and perspectives on possible future work in Sect. 5.

2 Response to concentrated loads of a suitably pre-stressed shell

The structure studied is a pre-stressed shell made of a composite laminate shown in Fig. 1 (more details on the material are given in Sect. 3.1). In its natural stress-free configuration, the shell has a rectangular planform Ω with sides L_x and L_y ; one side of the shell has curvature h_1 , while the other is flat, see Fig. 1A. Once the curved side is clamped, the shell equilibrium shape is changed into the curved profile shown in Fig. 1B. This equilibrium shape is associated with a relevant stress field which is the principal responsible for the nonlinear elastic behavior of such a structure. We refer the interested reader to [18,27,28] where a similar class of shells subject to clamped boundary conditions was extensively studied.

In the case studied, the natural configuration (namely h_1) is chosen such that the shell is monostable after clamping, but can become bistable after the application of external loads. As anticipated, this is the novelty of our approach, since bistability is not induced by means of complex phenomena or actuations, but it is rather obtained, in a reversible manner, only as a result of suitable loading conditions.

To understand more precisely such a nonlinear behavior, we discuss the shell response under the application of a dead load at its tip. Specifically, in Fig. 2, we plot the vertical displacement w of the shell tip versus the intensity of the vertical force F .

When the applied force F is sufficiently low, there is only one equilibrium branch stemming from the curved equilibrium shape shown in Fig. 1B (here represented by the point $w = 0$). When increasing the force, we reach a threshold value ($F = F_A$) where this equilibrium branch becomes unstable: the shell snaps into a second equilibrium branch which is the only stable one for forces higher than F_A . From Fig. 2, one can see that the shape of the shell once snapped is nearly flat (i.e., small displacements with respect to the XY plane). In the context of a uniform air flow in the X direction (our working condition in the experiments, see Fig. 1), we can thus denote the initial branch as a branch of “high-drag” configurations, and the second branch one of “low-drag” configurations. If starting from $F > F_A$ (therefore from a point on the snapped branch), we decrease the applied force we reach another threshold value ($F = F_B$) where the snapped branch becomes unstable. The shell configuration is hence forced to snap back to the initial equilibrium branch. Note that, the structural behavior along the equilibrium branches is elastic and reversible; however, the two jumps at $F = F_A$ and $F = F_B$ are not reversible and have well-definite directions shown by the arrows in Fig. 2. Therefore, if we consider a load cycle $0 \rightarrow \bar{F} > F_A \rightarrow 0$, the structure undergoes a hysteresis loop where energy is dissipated. This dissipated energy corresponds to the area enclosed by the loop in the Figure.

The equilibrium points of Fig. 2 can be computed using the reduction procedure discussed in [19]. The result is an analytic expression for the total energy which, once minimized, gives the stable equilibria corresponding to each value of the external force F .

The described dead-load experiment is the only one allowing for a simple semi-analytic solution but serves as motivation for the rest of the work where the follower force is substituted with an aerodynamic, distributed load.

Indeed, we aim to verify, both experimentally and numerically, the nonlinear response of Fig. 2 under the application of a realistic aerodynamic load. In particular, we consider the shell embedded in a high Reynolds flow having undisturbed velocity at infinity $U_\infty \mathbf{a}_X$ aligned along the shell axial direction, see Fig. 1B. The airflow forces are expected to trigger the shell transition toward a more streamlined shape (snapped branch), where the drag sensibly drops. Given the completely passive mechanism that drives the shape transition, the proposed pre-stressed structure can have relevant applications as a morphing aileron for drag reduction.

3 Materials and methods

3.1 Material specification

The prototype shell is made of a composite laminate, realized with the stacking of 8 layers (0.125mm thick). Each layer is a unidirectional carbon ply of epoxy resin (TenCate TC275-1), cured at 135 °C, see [28]. The stacking sequence of the layers is as follows:

$$[-\alpha / +\alpha / +\alpha / -\alpha / +\alpha / -\alpha / -\alpha / +\alpha], \quad (1)$$

with $\alpha = 45^\circ$ the principal orthotropy direction of each ply, with respect to the axial direction of the shell. The chosen number of layers and stacking sequence are a sufficient condition for designing un-coupled, quasi-homogeneous orthotropic laminates. The angle α can then be tuned to obtain the desired behavior: choosing

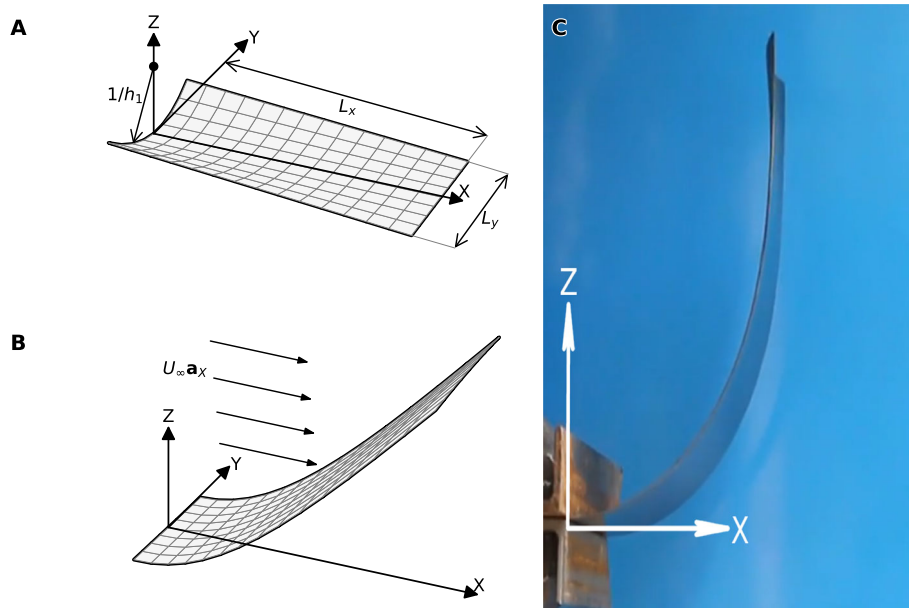


Fig. 1 **A** Natural stress-free configuration of the shell. **B** Equilibrium shape after clamping the curved side. Later a flow in the axial direction, having velocity $U_\infty \mathbf{a}_x$ will be considered. **C** Actual snapshot of the prototype after clamping

$\alpha = 45^\circ$ yields a bistable shell and allows for a starting shape (when clamped) which is well suited for our purposes. As a result of the choices above, one can use the Classical Laminated Plate Theory to derive the homogenized stiffness matrices to be used in the derivation of the elastic energy, see [28] for details. The curvature of the $X = 0$ side in the stress-free configuration, see Fig. 1A, is $h_1 = 15.625 \text{ m}^{-1}$. The resulting thickness is 1 mm with planform sides $L_x = 0.33 \text{ m}$ and $L_y = 0.15 \text{ m}$.

3.2 Experimental setup

An experimental campaign was run in the wind tunnel facility available at the Fluid Mechanics Lab at the Sapienza University of Rome. The wind tunnel has a closed loop configuration with an open circular test section of diameter $D = 1 \text{ m}$, and maximum free-stream velocity of 40 m/s. The air speed in the test section is measured with a Pitot tube, and a dynamometric scale with three load cells is used to measure the forces acting on the aileron. The pre-stressed clamped aileron shown in Fig. 1C is placed at the center of the wind tunnel thanks to a supporting beam. The beam, visible on the right of Fig. 4, is sufficiently thin to have a modest aerodynamic interaction with the flow and sufficiently stiff to maintain the initial angle of attack. Indeed, during the experimental runs described below, a maximum rotation angle of about 3 degrees has been recorded. During each experimental run, the air speed U_∞ was varied, in a controlled manner, with small increments from 0m/s up to 32m/s to ensure an almost quasi-static loading of the shell. Preliminary tests performed in a reduced range of airspeed with different values of increment ΔU_∞ exclude any bias in the results due to the loading history. The drag force on the aileron is gauged every 5 m/s, when the velocity increase is temporarily stopped to ensure stationary conditions at the moment of measurement. The selected velocity range was sufficient to observe in a robust way the transition to the snapped “low-drag” configuration. Once the snap to the “low-drag” configuration takes place, we similarly decrease the velocity back to zero. Concerning the identification of the critical velocity at which the snaps occur, independent measurements have been performed by using a Pitot tube by varying the fluid velocities around the expected values. These multiple measurements allow us to reduce the error in the velocity prediction. It is worth noting that the orientation of the aileron with respect to the flow direction and to the balance axis allows us to only measure the aileron drag, while the lift exerted by the system is not accessible in the present configuration. We stress however that the measure of the lift is out of the goal of the present manuscript.

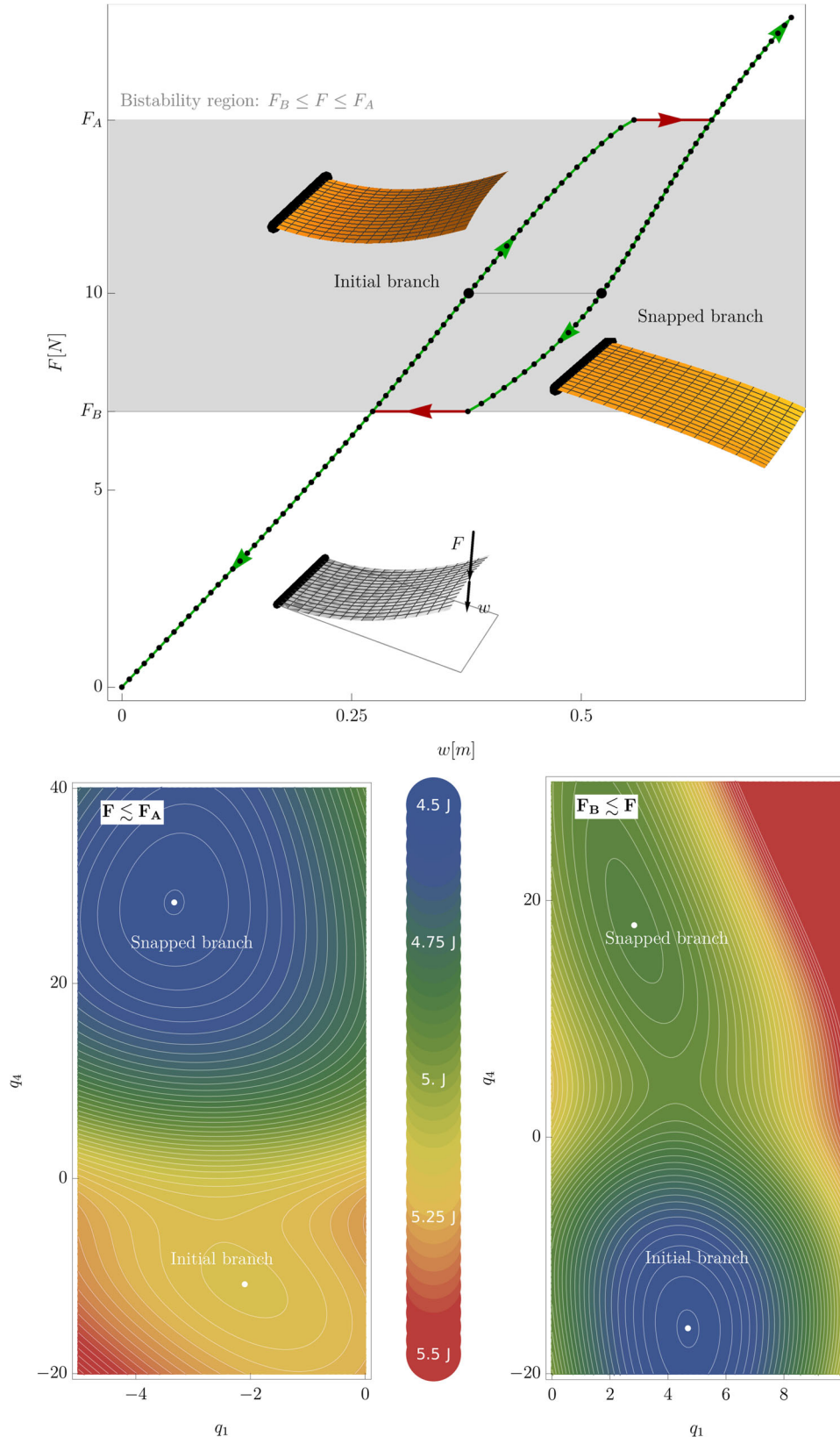


Fig. 2 *Top:* Vertical displacement w of the clamped shell tip as function of a vertical follower load F . Green arrows indicate reversible paths while red arrows indicate the jumps to and from the snapped configuration. *Bottom:* contour plots in the plane (q_1, q_4) of the elastic energy $\min_{q_3} \mathcal{E}_e(q_1, q_3, q_4)$ for F just below the threshold F_A (left) and for F just above the threshold F_B (right)

3.3 Numerical setup

Together with the experiments, we also performed numerical simulations to investigate the potential of the numerics in reproducing the actual aileron behavior, with particular attention to the prediction of the threshold velocity U_∞^A . Given the relatively complex geometry of the body and the high Reynolds number flow, the fluid dynamics is studied using the Reynolds Averaged Navier–Stokes (RANS) approach. Remark that RANS solutions can effectively reproduce statistically steady flow fields, which are reasonably expected to occur for the whole velocity range considered, except near the threshold velocities where relevant oscillations take place. The structural solver models the aileron as a nonlinear shell with a reduced energy functional with only 3 Lagrangian parameters. These are sufficient to determine both the structural 3D shape and the stored elastic energy [29]. The aeroelastic problem is split into the subsequent solution of the structural and aerodynamic problems, see Algorithm 1, until convergence is reached. To reproduce the experimental runs, starting from the flow acceleration phase we do the following: Each simulation starts from the clamped undeformed aileron configuration and zero free-stream velocity. The free-stream velocity is then set to the desired value U_∞ , and the steady-state aerodynamic loads from the RANS simulations are computed and used to determine a new equilibrium configuration of the aileron. The procedure is repeated until reaching convergence within the required tolerances. For some (high) values of free-stream velocity, we check that the same result is obtained if instead the inlet velocity is increased progressively by $\Delta U_\infty = 1 \text{ m/s}$, starting from zero, up to the desired value. A similar procedure is followed when, for high-flow velocities, we find the emergence of another stable equilibrium solution: we take it as the new starting configuration and apply incremental variations ΔU_∞ , in order to determine its stability range. The basic ingredients to solve the aeroelastic interaction are the solution of the structural system with given aerodynamic forces and the solution of the RANS equations with a prescribed shape of the structure, i.e., the geometry of the body. In the following, we describe these two sub-problems.

3.3.1 Structural subsystem

We suppose that the aerodynamic contact force on every element of the shell surface is known. In general, as the fluid is viscous, we decompose the aerodynamic force per unit area as follows:

$$\mathbf{F} = p \mathbf{n} + \mathbf{f}, \quad \mathbf{f} \cdot \mathbf{n} = 0, \quad (2)$$

where \mathbf{n} is the normal to the shell mid-surface, see Eq. (12) below, p is the pressure field, and \mathbf{f} is the tangential component of the aerodynamic load (viscous stress).

The structure is modeled as a nonlinear Koiter shell; as such, using a Lagrangian approach, its kinematical descriptors are the normal, u , and membranal, v , components of the displacement in every point of the planform Ω . The shell behavior is governed by an assignment of the elastic energy $\mathcal{E}_K(u, v)$.

However, to simplify the structural operator, we use a special ansatz for the displacement fields, say $u = \hat{u}(\mathbf{q})$ and $v = \hat{v}(\mathbf{q})$, to deduce a reduced elastic energy $\mathcal{E}_e(\mathbf{q}) = \mathcal{E}_K(\hat{u}(\mathbf{q}), \hat{v}(\mathbf{q}))$ given in terms of only 3 Lagrangian parameters $\mathbf{q} = (q_1, q_3, q_4)$. This is done following the procedure extensively discussed in [19, 27]. The Lagrangian parameters have the following meaning, respectively: q_1 the curvature near the clamp of the shell center line $Y = 0$, q_3 the gradient of curvature along the center line and q_4 a measure of the Y -curvature of the shell cross-section. In particular, the average curvature of the center line is given by $q_1 + q_3 L_x/2$.

Once the aerodynamic force \mathbf{F} corresponding to the configuration \mathbf{q}_o is known, the updated structural configuration \mathbf{q}^* is computed minimizing the total energy

$$\mathbf{q}^* = \operatorname{argmin}_{\mathbf{q}} \mathcal{E}(\mathbf{q}, \mathbf{F}, \mathbf{q}_o), \quad \mathcal{E}(\mathbf{q}, \mathbf{F}, \mathbf{q}_o) := \mathcal{E}_e(\mathbf{q}) - \mathcal{L}_{ext}(\mathbf{q}, \mathbf{F}, \mathbf{q}_o), \quad (3)$$

where the work of aerodynamic forces is defined as usual as

$$\mathcal{L}_{ext}(\mathbf{q}, \mathbf{F}, \mathbf{q}_o) := \int_{\mathbf{q}_o}^{\mathbf{q}} \mathbf{Q}(\mathbf{F}, \mathbf{q}) \cdot \delta \mathbf{q}, \quad (4)$$

with $\mathbf{Q}(\mathbf{F}, \mathbf{q})$ the vector of Lagrangian forces having components

$$Q_j(\mathbf{F}, \mathbf{q}) = \int_{\Omega} \mathbf{F} \cdot \frac{\partial(\mathbf{u}\mathbf{n} + \mathbf{v})}{\partial q_j} = \int_{\Omega} \left(p \frac{\partial \hat{u}(\mathbf{q})}{\partial q_j} + \mathbf{f} \cdot \frac{\partial \hat{\mathbf{v}}(\mathbf{q})}{\partial q_j} \right) d\Omega, \quad j = 1, 3, 4. \quad (5)$$

To compute the work of aerodynamic forces, one must evaluate the path integral in (4); clearly, the work depends on the path followed from \mathbf{q}_o to \mathbf{q} . This is due to the fact that also the aerodynamic forces depend on

the configuration. If \mathbf{q}_o and \mathbf{q} are not too far, we can approximate the work, choosing a straight path between them

$$\mathcal{L}_{ext} \simeq \int_0^1 \mathbf{Q}(\mathbf{q}_o + t(\mathbf{q} - \mathbf{q}_o)) \cdot (\mathbf{q} - \mathbf{q}_o) dt \simeq \left[\frac{\mathbf{Q}(\mathbf{F}_o, \mathbf{q}_o)}{4} + \frac{3}{4} \mathbf{Q}\left(\mathbf{F}_o, \frac{2\mathbf{q} + 3\mathbf{q}_o}{3}\right) \right] \cdot (\mathbf{q} - \mathbf{q}_o) \quad (6)$$

where we have used the quadrature formula

$$\int_0^1 f(t) dt \simeq \frac{1}{4} f(0) + \frac{3}{4} f\left(\frac{2}{3}\right), \quad (7)$$

exact for second-order polynomials. The minimum of (3) is found with a standard Quasi-Newton method starting from $\mathbf{q} = \mathbf{q}_o$.

3.3.2 Fluid subsystem: RANS simulations

We suppose given the structural configuration \mathbf{q}_o ; in other words, using these Lagrangian parameters introduced previously, we reconstruct the shell mid-surface and, from it, using the thickness t , the solid shape of the aileron. To this aim, first we introduce the angle of the centerline in the XZ plane,

$$\theta(X) = q_1 X + q_3 \frac{X^2}{2}, \quad X \in [0, L_x]. \quad (8)$$

and recall that the curvature of the center line is given as the derivative:

$$\chi(X) = \theta'(X) = q_1 + q_3 X, \quad X \in [0, L_x]. \quad (9)$$

We then deduce through integration the 3D centerline of the aileron

$$\mathbf{c}(X) = \int_0^X (\cos \theta(s) \mathbf{a}_X + \sin \theta(s) \mathbf{a}_Z) ds. \quad (10)$$

having used the clamping condition $\theta(X=0) = 0$ and the unit vectors $\mathbf{a}_X, \mathbf{a}_Z$ of the X, Z axes, see Fig. 1A. Hence, using the Lagrangian parameter q_4 , meaning the transverse curvature, we deduce the mid-surface of the shell as

$$\mathbf{S}(X, Y) = \mathbf{c}(X) + Y \mathbf{a}_Y + q_4 \frac{Y^2}{2} \mathbf{m}(X), \quad X \in [0, L_x], Y \in [0, L_y], \quad (11)$$

where $\mathbf{m}(X) = -\sin \theta(X) \mathbf{a}_X + \cos \theta(X) \mathbf{a}_Z$ is the normal to the center line. Given the mid-surface $\mathbf{S}(X, Y)$, we use the normal vector field, defined as

$$\mathbf{n}(X, Y) = \frac{\mathbf{g}_X \times \mathbf{g}_Y}{\|\mathbf{g}_X \times \mathbf{g}_Y\|}, \quad \text{with} \quad \mathbf{g}_X = \frac{\partial \mathbf{S}(X, Y)}{\partial X}, \quad \mathbf{g}_Y = \frac{\partial \mathbf{S}(X, Y)}{\partial Y}, \quad (12)$$

to thicken the shell and to define its upper and lower surfaces: $\mathbf{S}(X, Y) \pm \mathbf{n}(X, Y) t/2$. With these surfaces, we define a solid shape, namely an STL file, which is used by the *snappyHexMesh* utility of the *OpenFOAM* numerical library (<https://openfoam.org>) to generate a mesh for the fluid domain. The resulting fluid domain consists of a three-dimensional box with an internal boundary which coincides with that of the structure in the configuration that is to be studied. The origin is centered at the midpoint of the clamped side, as shown in Fig. 1A. The box size is large enough to mimic free space conditions as in the experiments. A sketch of the computational domain is given in Fig. 3, where the sizes are normalized with respect to the side lengths of the aileron planform, shown in Fig. 1A. Panels B and C of Fig. 3 show two 2D cuts close-up views of the 3D computational domain that cross the body at the midsection. We adopted a first refinement box that extends upstream and further downstream the aileron in order to accommodate the wake behind the bluff body. This is crucial since the aerodynamic loads are greatly affected by the resolution of the vorticity field behind the body. As a second level of refinement, see panel C, the mesh is morphed into the actual body shape by adding wall-parallel layer cells. Again, this is crucial to enforce the correct boundary conditions on solid boundaries that are essentially based on our understanding of turbulence in parallel flows [30]. The average cell size is about $0.1L_x$ at the coarser level and $0.05L_x$ in the first refinement box, while the average boundary layer

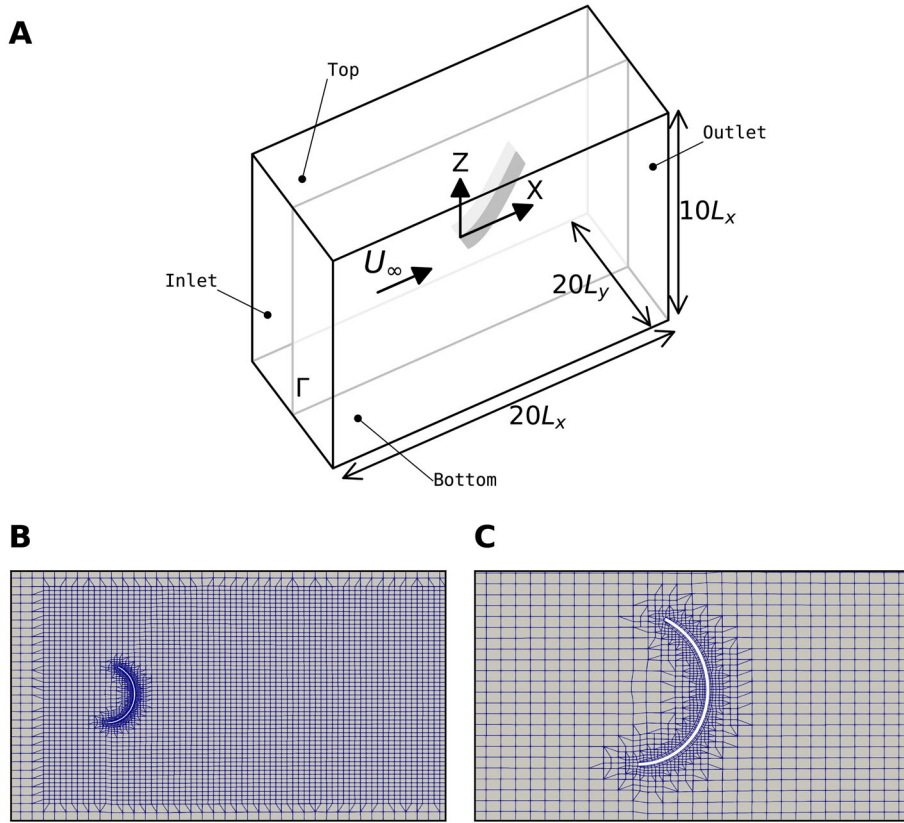


Fig. 3 Computational domain for the numerical simulations of steady flow around the aileron. **A** Sketch of the domain, boundaries not labeled are the planes of symmetry. **B**, **C** Detail of the mid-section plane of the domain indicated with Γ in the sketch

element thickness, at the body surface, is about $0.006L_x$, where sizes are again normalized with respect to the length of the aileron planform.

The fluid flow is solved by the *OpenFOAM* library assuming steady Reynolds Averaged Navier–Stokes (*RANS*) equations; specifically, we use the *simpleFoam* solver, suitable for computation of the stationary solutions. This allows, at any given velocity U_∞ and solid shape \mathbf{q}^k , to estimate the aerodynamic forces

$$\mathbf{F}^{k+1} = p^{k+1} \mathbf{n}^k + \mathbf{f}^{k+1} = \mathcal{F}(U_\infty, \mathbf{q}^k) \quad (13)$$

The *RANS* model provides the mean field variables of a fully developed turbulent flow. Indeed, a rough estimate of the magnitude of the incoming flow velocity necessary to produce the snap of the aileron can be computed by equating the tip force F_A computed in Fig. 2 to the drag force over a flat plate with the same dimensions of the structure. Since $F_A \simeq 10 \div 15$ N, assuming a unitary drag coefficient, we estimate a Reynolds number of the order of $10^5 \div 10^6$, meaning that the flow is expected to be fully turbulent. In the simulations, the standard $k - \varepsilon$ turbulence model is adopted. At the inlet, the free-stream velocity is prescribed while on the aileron surface no-slip and impermeability conditions are enforced. The Neumann boundary condition is assigned for the velocity at the outlet. The top and bottom surfaces (w.r.t. the Z direction) of the computational box are modeled as walls, where a *slip* boundary condition is assigned on the velocity (i.e., the velocity is forced to be tangential to the domain boundary). The two remaining surfaces are set as symmetry planes. Concerning the pressure, a fixed value of 0 is set at the outlet while the Neumann boundary condition is assigned to the rest of the boundaries of the domain. Standard wall functions are used to enforce the boundary conditions for the turbulent kinetic energy k and for the energy dissipation rate ε at solid boundaries, and to correct the turbulent eddy viscosity in the near wall region in order to model the boundary layer. The inlet values of the turbulent kinetic energy and dissipation are assigned assuming a free-stream isotropic turbulent flow, namely

$$k_\infty = \frac{3}{2} u_{rms}^2 = (I U_\infty)^2, \quad \varepsilon_\infty = \frac{1}{L_y} \left(\frac{2}{3} k_\infty \right)^{3/2}. \quad (14)$$

where $I = 0.1$ is the turbulence intensity, and L_y is the length of the shell planform taken as reference integral length-scale of the turbulent fluctuations. The standard OpenFOAM values of the constants involved in the model were used. We verified a posteriori, from the simulation data, that the location of the first grid point away from the aileron wall is such that the y^+ value is in the range [80–200], which corresponds to a correct usage of the turbulent boundary conditions and wall functions. This choice of turbulence model is suitable for our goals, while a LES model would be more appropriate if one wished to simulate the entire unsteady process accurately. The discretization of the Navier–Stokes equations in *simpleFoam* exploits a finite volume method, resulting in a second-order accuracy for regular meshes. The discretization of numerical fluxes of all variables uses a TVD interpolation method ensuring a solution free from oscillations, thus achieving a more rapid convergence. We employ schemes in their *bounded* variants, having additional terms used to penalize the continuity (incompressibility) errors. These terms added to the discretized equations are consistent in that they vanish when convergence to a solution is reached.

Algorithm 1 Sub-iteration scheme

```

n = 0, U∞0 = 0, qn = q0.
for n ∈ (1, . . . , N) do
  U∞n = U∞n-1 + nΔU, k = 0, qn,0 = q0
  while ||qn,k - qn,k-1|| > ε do
    Fn,k+1 = F(U∞n, qn,k)
    qn,k+1 = argminq E(q, Fn,k+1, qn,0)
    k ← k + 1
  end while
  qn ← qn,K, Fn ← Fn,K.
end for

```

▷ ε convergence threshold
 ▷ See Eq. (13)
 ▷ See Eq. (3)
 ▷ K last iteration value

4 Results and discussion

4.1 Experimental results

In Fig. 4, we plot the measured drag versus the flow velocity U_∞ for two experimental campaigns at a distance of a few days. The points shown are an average of the measured values for each free-stream velocity value. The data dispersion is represented by the corresponding error bars. Note that the drag is rescaled as the drag coefficient $C_D = D/(1/2\rho AU_\infty^2)$, with A the area of the planform of the shell, to better appreciate the transition between the “high-drag” and the “low-drag” configurations of the aileron. On the right of the same Figure, a superposition of several snapshots of the aileron is shown: a sequence of continuously deformed high-drag configurations and the snapped low-drag configuration (thick white line) is clearly visible. Starting from $U_\infty = 4$ m/s and by increasing the airspeed the drag coefficient slightly increases to remain almost constant until some critical velocity is reached, where a sudden drop of C_D is observed. This corresponds to the threshold value for transition “A” toward the low-drag configuration at $U_\infty^A = 29 \pm 2.5$ m/s; during this transition, the drag suddenly decreases by a factor of about 5. Before reaching the snap speed, the variation of the frontal area of the body is rather small, hence the almost constant values of the drag coefficient. In principle, the “low-drag” configuration is stable for velocities much greater than U_∞^A . For the present purposes, we continued to increase the velocity up to 32 m/s without observing any change in the aileron configuration. Starting from the maximum velocity reached in the experiment, i.e., 32 m/s, by decreasing the airspeed, see the low drag data in Fig. 4, the reverse transition “B” from the low-drag back toward the high-drag configuration is observed at $U_\infty^B = 17 \pm 2.5$ m/s.

Several independent measurements of this cycle loop have been performed, paying particular attention to the identification of the threshold velocities and their reproducibility. The reader can find from the References two videos [31,32] illustrating the transition from the high-drag toward the low-drag configuration and vice versa.

Remark from the video that when approaching the critical velocities U_∞^A and U_∞^B the aileron undergoes relevant oscillations. This is caused by a vanishing tangent operator of the coupled aeroelastic system; close to these velocities the flow is no longer stationary and the inertia forces play a relevant role. However, as soon as the transitions take place, we recover the quasi-static stationary conditions for the system. These oscillations

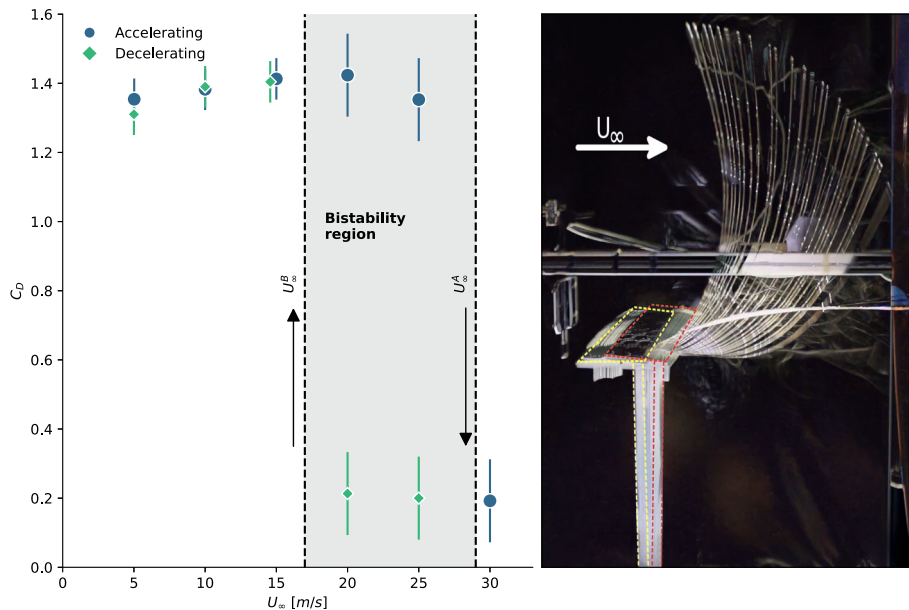


Fig. 4 Left: experimental results in terms of measured drag coefficient, as a function of the external flow velocity. Right: superposition of snapshots of an experimental run in the wind tunnel, during an acceleration of the external flow until the shell snaps to a different stable configuration

do not appear in Fig. 4 because the drag force is averaged by the load cells of the scale at each velocity regime. It is interesting to compare the magnitudes of the force that induces the snap-through for the point load case of Sect. 2 and of the maximum experimental load: in experiments, the maximum value of drag recorded prior to the snap-through was approximately 25 N, while in Fig. 1 one can infer a maximum (follower) force of around 15 N.

4.2 Numerical results

The aeroelastic coupling is solved according to the alternate solution of the structural and aerodynamic problems sketched in Algorithm 1, where we choose a convergence threshold $\varepsilon = 1e^{-5}$ on the variation of the Lagrangian parameters. We remark that, starting from the simulation of the flow acceleration phase, for each value of the velocity at infinity U_∞ , the iterative process is started from the rest configuration \mathbf{q}_0 (corresponding to zero external force), rather than the one obtained from the solution at the last step. We check, for some of the data points, that this procedure yields the same results as the incremental one, i.e., increasing the free-stream velocity in smaller increments, reaching convergence each increment, and using the intermediate solution as the starting configuration for the following step. In this way, we ensure that there is no bias in the procedure due to non-convergence errors accumulated along each step in the sequence. This is in agreement with our goal of finding stable stationary solutions corresponding to a given velocity range, and the fact that we employ a steady flow solver. Convergence is easily attained with few iterations for most far-field velocity values U_∞ in the considered range, except for the steps that immediately precede the snap-through transition. In these cases, the average number of iterations is higher (order 10), due to the oscillating behavior that naturally occurs during such transitions. The incoming flow at infinity is oriented in the X direction (see Fig. 1A), therefore impinging the surface as a bluff body when this is curled after clamping, see inset A in Fig. 5 (relative to the case $U_\infty = 17$ m/s), for velocities up to $U_\infty \simeq 15 \div 17$ m/s. Within this range of velocities, from the aerodynamic point of view, we observe the typical bluff body flow separation characterized by an intense vorticity release in the wake behind the body. The drag force D (direction X) is almost constant once normalized with U_∞^2 , while the intensity of the normalized lift force L (direction Z) grows, see the main panel of Fig. 5 where the numerical data are compared against the experimental measurements. Surprisingly the numerical results are in fairly good agreement with the experimental data on the drag forces in almost the entire range of velocities without requiring any special tuning of the $k - \varepsilon$ model parameters. For velocities in the range [17, 29] m/s, we observe a progressive flattening of the aileron and an almost absent separation, see inset B in Fig. 5. While

Table 1 Numerical and experimental results

	Minimum C_D	Maximum C_D	Threshold U_∞^A [m/s]	Threshold U_∞^B [m/s]
Experimental	0.19	1.44	29.5	17.0
Numerical	0.23	1.50	32.0	–

the experimental evidence shows a sudden drop of the drag force for velocities around $U_\infty^A = 29\text{m/s}$, the drag force as predicted by the numerical simulations decreases smoothly between the experimental limit values $D = 0.045 U_\infty^2$ N and $D = 0.005 U_\infty^2$ N, for free-stream velocity up to 32 m/s. Increasing the value of U_∞ further, we observe a phase of important oscillations and difficult convergence, before the aileron stabilizes into a completely flat shape, inset C in Fig. 5. Insets B and C are relative to the two equilibria found for free-stream velocity $U_\infty = 29$ m/s. This flat configuration remains stable when increasing the velocity to higher values (we checked up to $U_\infty = 35$ m/s). Then, using this configuration as the starting condition and varying U_∞ , we find that it is stable also when decreasing the free-stream velocity, down to values considerably lower than the U_∞^B threshold. This behavior poses the question of how to identify the “numerical” transition velocity. We assume that the threshold U_∞^A coincides with the free-stream velocity for which the numerical procedure starts exhibiting oscillating behavior. Therefore, we estimate $U_\infty^A = 32$ m/s, which falls within the variability interval of the experimental measures.

The numerical estimates of the drag force of the snapped configuration are in very good agreement with the experimental results, until the experimental velocity threshold U_∞^B .

The implemented numerical scheme is able to capture the limit values for the drag forces and to indicate the threshold velocity for the snap instability, but it is not able to reproduce the sudden drop in the drag force, and the snap-back to the starting equilibrium branch for the U_∞^B threshold. In Table 1 we report a comparison between experimental and numerical results. As expected, the instability phase is not faithfully captured due to the use of both a reduced model for the shell and a steady-state mean flow field solution. The current model is refined enough to reproduce the stability landscape in the (steady) case of an idealized follower load reported in Sect. 2, where the external Lagrangian force is constant, but the case of an aerodynamic load considered here is more challenging. Indeed, we believe that the transition is triggered by unsteady and intense turbulent fluctuations that are out of the range of the present RANS solution. A much more relevant computational effort would be needed to cure these aspects, considering more degrees of freedom in the structural system, and a more reliable description of the flow including unsteady effects that can be captured by, e.g., Detached Eddy Simulations or Large Eddy Simulations. One could also couple and solve the structural and fluid subsystems monolithically to improve the accuracy, especially close to snap points where the structure deforms at high rates. This however would require the knowledge of the tangent operator of the two systems of PDEs, and therefore either a complete rewrite from scratch of the solvers and of the algorithm, or the introduction of some sort of approximation of these operators, in both cases adding another layer of complexity.

5 Conclusions

We have presented an original setup for a smart aileron proving valuable for drag reduction strategies. A suitably curved shell is clamped and, therefore, pre-stressed in order to produce a peculiar multi-stable behavior under aerodynamic flows. Such a shell has only one stable equilibrium (with the relevant drag) at low velocities and another different equilibrium branch (with the vanishing drag) at high velocities. The two branches superpose for the intermediate regimes. Hence, such an aileron snaps in the low-drag configuration when the flow velocity surpasses a given threshold, but it is able to retrieve the initial configuration without any actuation when the flow slows down. We first predicted a similar behavior numerically using a point follower load with a few degrees of freedom model for the shell. Then, with an experimental campaign in the wind tunnel, we confirmed that also aerodynamic forces can trigger the same bistable and reversible behavior. Numerically solving an aeroelastic problem where the shell is coupled to the quasi-static Navier–Stokes equations, we are also able to estimate the limit values for the drag and lift forces and the critical velocity at which the aileron snaps. Using more accurate yet discrete shell models and considering the inertia forces, while dismissing the quasi-static hypothesis, could improve the description of the aeroelastic interaction near the snap instability. Further developments of a similar concept could also include a complete assignment of the initial and snapped aileron configuration including torsional deformations. Another research topic would concern the dynamics of these

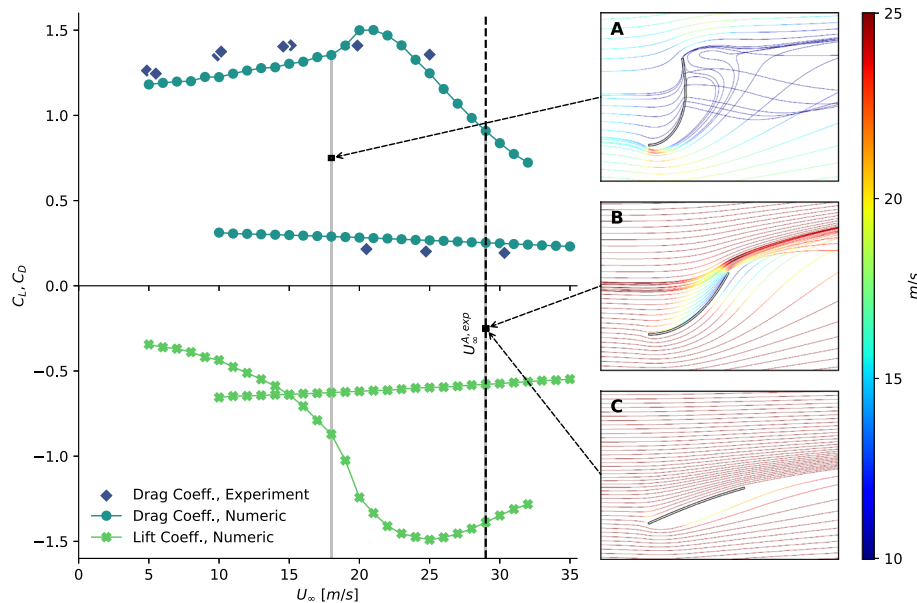


Fig. 5 Left: Numerical results, given as a function of the outer flow velocity. Drag coefficient, C_D (force in X direction) and lift coefficient, C_L (force in Z direction). Right: snapshots of streamlines, from numerical simulations, on a plane intersecting the structure at the middle ($Y = 0$). Color intensity scale is based on the axial velocity (X direction) value

bistable plates: in [29], the large amplitude nonlinear behavior of this class of shells is studied both theoretically and experimentally, for harmonic forcing. It would be interesting to perform a similar analysis in our context, with possible energy harvesting applications in mind.

Acknowledgements GC and SV were supported by the Project BIT4MaPS PoC: AERO-elastic response of pre-stressed MORPHing shells - Aeromorph (Ministero dello Sviluppo Economico).

Open Access This article is licensed under a Creative Commons Attribution 4.0 International License, which permits use, sharing, adaptation, distribution and reproduction in any medium or format, as long as you give appropriate credit to the original author(s) and the source, provide a link to the Creative Commons licence, and indicate if changes were made. The images or other third party material in this article are included in the article's Creative Commons licence, unless indicated otherwise in a credit line to the material. If material is not included in the article's Creative Commons licence and your intended use is not permitted by statutory regulation or exceeds the permitted use, you will need to obtain permission directly from the copyright holder. To view a copy of this licence, visit <http://creativecommons.org/licenses/by/4.0/>.

Funding Open access funding provided by Università degli Studi di Roma La Sapienza within the CRUI-CARE Agreement.

References

1. Bhattacharya, K., James, R.D.: The material is the machine. *Science* **307**(5706), 53–54 (2005). <https://doi.org/10.1126/science.1100892>
2. McCracken, J.M., Donovan, B.R., White, T.J.: Materials as machines. *Adv. Mater.* **32**(20), 1906564 (2020). <https://doi.org/10.1002/adma.201906564>
3. Sun, J., Guan, Q., Liu, Y., Leng, J.: Morphing aircraft based on smart materials and structures: a state-of-the-art review. *J. Intell. Mater. Syst. Struct.* **27**(17), 2289–2312 (2016). <https://doi.org/10.1177/1045389X16629569>
4. Loewy, R.G.: Recent developments in smart structures with aeronautical applications. *Smart Mater. Struct.* **6**(5), 11 (1997). <https://doi.org/10.1088/0964-1726/6/5/001>
5. Gomez, J.C., Garcia, E.: Morphing unmanned aerial vehicles. *Smart Mater. Struct.* **20**(10), 103001 (2011). <https://doi.org/10.1088/0964-1726/20/10/103001>
6. Simiriotis, N., Jodin, G., Marouf, A., Elyakime, P., Hoarau, Y., Hunt, J.C.R., Rouchon, J.F., Braza, M.: Morphing of a supercritical wing by means of trailing edge deformation and vibration at high reynolds numbers: experimental and numerical investigation. *J. Fluids Struct.* **91**, 102676 (2019). <https://doi.org/10.1016/j.jfluidstructs.2019.06.016>
7. Hu, N., Burgueño, R.: Buckling-induced smart applications: recent advances and trends. *Smart Mater. Struct.* **24**(6), 063001 (2015). <https://doi.org/10.1088/0964-1726/24/6/063001>

8. Ahsan, S.N., Aureli, M.: Nonlinear oscillations of shape-morphing submerged structures: control of hydrodynamic forces and power dissipation via active flexibility. *J. Fluids Struct.* **74**, 35–52 (2017). <https://doi.org/10.1016/j.jfluidstructs.2017.06.010>
9. Barbarino, S., Flores, E.S., Ajaj, R.M., Dayyani, I., Friswell, M.I.: A review on shape memory alloys with applications to morphing aircraft. *Smart Mater. Struct.* **23**(6), 063001 (2014). <https://doi.org/10.1088/0964-1726/23/6/063001>
10. Bin, J., Oates, W.S., Yousuff Hussaini, M.: Fluid-structure interactions of photo-responsive polymer cantilevers. *J. Fluids Struct.* **37**, 34–61 (2013). <https://doi.org/10.1016/j.jfluidstructs.2012.10.008>
11. Kim, J., Kim, H., Kim, D.: Snap-through oscillations of tandem elastic sheets in uniform flow. *J. Fluids Struct.* **103**, 103283 (2021). <https://doi.org/10.1016/j.jfluidstructs.2021.103283>
12. Multi-parameter actuation of a neutrally stable shell: a flexible gear-less motor. *Proceedings of the Royal Society A: Mathematical, Physical and Engineering Sciences* **473**(2204), 20170364 (2017)
13. Corsi, G., De Simone, A., Maurini, C.: A neutrally stable shell in a stokes flow: a rotational taylor's sheet. *Proc. R. Soc. A* **475**(2227), 20190178 (2019)
14. Guest, S., Pellegrino, S.: Analytical models for bistable cylindrical shells. *Proc. R. Soc. A Math. Phys. Eng. Sci.* **462**(2067), 839–854 (2006)
15. Kebabdz, E., Guest, S., Pellegrino, S.: Bistable prestressed shell structures. *Int. J. Solids Struct.* **41**(11–12), 2801–2820 (2004)
16. Nicassio, F.: Shape prediction of bistable plates based on timoshenko and ashwell theories. *Compos. Struct.* **265**, 113645 (2021)
17. Yan, W., Yu, Y., Mehta, A.: Analytical modeling for rapid design of bistable buckled beams. *Theor. Appl. Mech. Lett.* **9**(4), 264–272 (2019)
18. Vidoli, S., Brunetti, M.: Method for making prestressed shells having tunable bistability. US Patent App. 17/254,003 (2021). International Patent WO 2019/244096 A1 (2019). Italian Patent N. 102018000006527 (2018)
19. Vidoli, S.: Discrete approximations of the föppl-von kármán shell model: from coarse to more refined models. *Int. J. Solids Struct.* **50**(9), 1241–1252 (2013). <https://doi.org/10.1016/j.ijsolstr.2012.12.017>
20. Mattioni, F., Gatto, A., Weaver, P., Friswell, M., Potter, K.: The application of residual stress tailoring of snap-through composites for variable sweep wings. In: 47th AIAA/ASME/ASCE/AHS/ASC Structures, Structural Dynamics, and Materials Conference. <https://doi.org/10.2514/6.2006-1972>
21. Mattioni, F., Weaver, P.M., Friswell, M.I.: Multistable composite plates with piecewise variation of lay-up in the planform. *Int. J. Solids Struct.* **46**(1), 151–164 (2009). <https://doi.org/10.1016/j.ijsolstr.2008.08.023>
22. Arrieta, A.F., Kuder, I.K., Rist, M., Waeber, T., Ermanni, P.: Passive load alleviation aerofoil concept with variable stiffness multi-stable composites. *Compos. Struct.* **116**, 235–242 (2014). <https://doi.org/10.1016/j.compstruct.2014.05.016>
23. Gosselin, F.P., De Langre, E.: Drag reduction by reconfiguration of a poroelastic system. *J. Fluids Struct.* **27**(7), 1111–1123 (2011)
24. Leclercq, T., Langre, E.: Drag reduction by elastic reconfiguration of non-uniform beams in non-uniform flows. *J. Fluids Struct.* **60**, 114–129 (2016)
25. Leclercq, T., Langre, E.: Reconfiguration of elastic blades in oscillatory flow. *J. Fluid Mech.* **838**, 606–630 (2018). <https://doi.org/10.1017/jfm.2017.910>
26. Marzin, T., Langre, E., Ramananarivo, S.: Shape reconfiguration through origami folding sets an upper limit on drag. *Proc. R. Soc. A* **478**(2267), 20220592 (2022)
27. Brunetti, M., Vincenti, A., Vidoli, S.: A class of morphing shell structures satisfying clamped boundary conditions. *Int. J. Solids Struct.* **82**, 47–55 (2016). <https://doi.org/10.1016/j.ijsolstr.2015.12.017>
28. Brunetti, M., Vidoli, S., Vincenti, A.: Bistability of orthotropic shells with clamped boundary conditions: an analysis by the polar method. *Compos. Struct.* **194**, 388–397 (2018). <https://doi.org/10.1016/j.compstruct.2018.04.009>
29. Brunetti, M., Mitura, A., Romeo, F., Warminski, J.: Nonlinear dynamics of bistable composite cantilever shells: an experimental and modelling study. *J. Sound Vib.* **526**, 116779 (2022)
30. Pope, S.B.: *Turbulent Flows*. Cambridge University Press, Cambridge (2000)
31. Videos of an experimental run in the wind tunnel. Transition to flat. <https://youtu.be/g-mG2goqXME>
32. Videos of an experimental run in the wind tunnel. Transition from flat. <https://youtu.be/kb31KZU4V4Q>